PASJ: Publ. Astron. Soc. Japan , 1–**??**, 出版日

Three-Dimensional Magnetohydrodynamic Simulation of Nonlinear Magnetic Buoyancy Instability of the Flux Sheet with Magnetic Shear

Satoshi Nozawa
Department of Science, Ibaraki University, Bunkyo 2-1-1 Mito, Ibaraki 310-8512
snozawa@env.sci.ibaraki.ac.jp

(Received 2005 February 0; accepted 受理日)

Abstract

Series of three-dimensional magnetohydrodynamic simulations are used to study the nonlinear evolution of the magnetic buoyancy instability of the magnetic flux sheet with magnetic shear. A horizontal flux sheet that is initially placed below the photosphere is susceptible to both the interchange instability and the Parker instability (the undular mode of the magnetic buoyancy instability). The growth rate in the linear stage of the instability in the numerical simulation is consistent with that predicted by the linear theory. In the nonlinear stage, the development depends on the initial perturbation form as well as the initial magnetic field configuration(i.e. presence of magnetic shear) When an initial perturbation is assumed periodic, the emerging flux rises up to the corona and the magnetic field expands like a potential field as in 2D results. When non-periodic perturbation or random perturbations are assumed initially, the magnetic flux expands horizontally when the magnetic field emerges a little into the photosphere. The distribution of magnetic field and gas tends to be in a new state of magnetohydrostatic equilibrium. When magnetic shear is present in the initial magnetic flux sheets, the interchange mode is stabilized so that the emerging loop becomes higher than in a no magnetic shear case. We also discuss how the presented results are related to the emerging flux observed on the Sun.

Key words: MHD–instabilities–plasma–Sun

1. Introduction

The magnetic activity observed on the Sun originates from the emergence of the magnetic flux which is created deep in the convection zone (e.g., Parker 1979). Sunspots and active regions are formed by the magnetic flux tubes emerging from the interior of the Sun into the solar atmosphere (e.g.,Zwaan 1985; Zwaan 1987) as a result of magnetic buoyancy (Parker 1955). Much of the dynamics of the emerging process of the magnetic field, however, is not yet understood well because of the intrinsic nonlinear properties. Hence it is important to study the nonlinear dynamics of emerging magnetic flux and magnetic buoyancy.

It has been revealed that a flux sheet in magnetohydrostatic equilibrium in a gravitationally stratified gas layer becomes unstable due to magnetic buoyancy. This is called the magnetic buoyancy instability (e.g., Hughes, Proctor 1988; Tajima, Shibata 1997). There are two modes in the magnetic buoyancy instability: the undular mode ($k \parallel \mathbf{B}$) and the interchange mode ($\mathbf{k} \perp \mathbf{B}$), where $\mathbf{k}$ is the wavenumber vector and $\mathbf{B}$ is the magnetic field vector. The undular mode is often called the Parker instability (Parker 1966) in astrophysical literatures, whereas the interchange mode is sometimes called the flute instability or the magnetic Rayleigh-Taylor instability (Kruskal, Schwarzchild 1954). The undular mode occurs for long-wavelength perturbations along the magnetic field lines (the most unstable wavelength $15H$, where H is the pressure scale height), when the magnetic buoyancy created by the gas sliding down along a field line is greater than the restoring magnetic tension. On the other hand, the interchange mode occurs for short-wavelength perturbations, when the interchange of two straight flux tubes reduces the potential energy in the system. The linear growth rate of the interchange mode is generally much greater than that of the undular mode because of the short wavelength, though the nonlinear stage is dominated by the undular mode in many cases (Matsumoto et al. 1993; Tajima, Shibata 1997). Hence, the undular mode (hereafter, called the Parker instability) is more important than the interchange mode in nonlinear problems, and therefore in astrophysical problems.

The first nonlinear simulations of the Parker instability were made by Matsumoto et al. (1988) using a two-dimensional (2D) MHD code. They found that giant interstellar clouds are formed in the nonlinear stage of the Parker instability, and that a shock wave is formed inside the downflow along the rising loop. Applying the Matsumoto et al. (1988) simulations to the solar case, Shibata et al. (1989b, 1990a) showed that the self-similar expansion of a magnetic loop occurs in the nonlinear evolution of the 2D Parker instability in the solar atmosphere (i.e., in the solar emerging flux). Nozawa et al. (1992)

have made an extensive study of the linear and nonlinear evolution of the Parker instability in the convectively unstable gas layer. Further 2D simulations have been done by Kamaya et al. (1996) for triggering the nonlinear instability by supernova explosion, and by Basu et al. (1997) and Kim et al. (2000) for application to galactic disks.

As shown by Parker (1966)'s original analysis, however, the most unstable mode shows three dimensional (3D) behavior. That is, the instability has the maximum growth rate for non-zero $k_\perp$ even when non-zero $k_\parallel$ is the main cause of the instability, where $k_\perp$ is the wavenumber vector perpendicular to the magnetic field and $k_\parallel$ is the wavenumber vector parallel to the magnetic field. Thus, 3D nonlinear simulations are necessary to examine the actual nonlinear evolution of the Parker instability in 3D space. Matsumoto, Shibata (1992) and Matsumoto et al. (1993) were the first works that performed 3D nonlinear simulations of the Parker instability for both solar and galactic cases, and confirmed the basic results of the previous 2D simulations, such as cloud formation, shock waves, self-similar evolution. However their spatial and temporal scales depended on $k_\perp$. If a large $k_\perp$ is initially assumed, the magnetic loop tends to have thinner structures and suffers from horizontal expansion, which eventually suppress the upward expansion (Matsumoto et al. 1993). Similar thinner structures have also been found in more recent 3D simulations by Kim et al. (1998a, 2001, 2002) and Hanasz et al. (2002).

However, if magnetic shear is present in the initial magnetized gas layer, the interchange mode is stabilized, i.e., the growth of thinner structures is suppressed and larger scale structures may appear (Hanawa et al. 1992). Kusano et al. (1998) using 2.5D MHD simulations showed that the larger scale structures are created in the presence of magnetic shear. Such magnetic shear is often observed in the solar active regions as twisted flux tubes (Kurokawa 1989; Kurokawa et al. 2002; Ishii et al. 1998; Matsumoto et al. 1998; Fan 2001; Magara, Longcope 2001; Ryu et al. 2003; Magara, Longcope 2003; Magara 2004; Fan, Gibson 2004), and may be created in the convection zone (Cattaneo et al. 1990; Matthews et al. 1995) and under the influence of the Coriolis force (Shibata, Matsumoto 1991; Chou et al. 1999; Hanasz et al. 2002). Nevertheless, no one has yet studied the effect of magnetic shear on the 3D nonlinear evolution of the Parker instability.

In this paper, by using 3D MHD simulations, we present a detailed analysis of the 3D nonlinear evolution of the Parker instability in a magnetic flux sheet with *magnetic shear*, and examine the effects of magnetic shear on the nonlinear Parker instability. The initial gas layer and magnetic field are assumed to be suitable for application to solar emerging flux (e.g., Shibata et al. 1989a), though the basic physics is also applicable to the galactic case. Section 2 gives assumptions, basic equations and numerical procedures. The numerical results are described in section 3, and section 4 is devoted to discussions and conclusions.

2. Methods of Numerical Simulations

2.1. Assumptions and Basic Equations

The assumptions, basic equations, and initial conditions are similar to those in Nozawa et al. (1992). That is, we assume the following: (1) the medium is an ideal MHD plasma, (2) the gas is a polytrope of index $\gamma = 1.05$, (3) the magnetic field is frozen into the gas, (4) the viscosity and resistivity are neglected.

Cartesian coordinates (x,y,z) are adopted so that the z-direction is anti-parallel to the gravitational acceleration vector. The gravitational acceleration is assumed constant. Thus, the basic equations in vector form are as follows:

$$\frac{\partial \rho}{\partial t} + \nabla \cdot (\rho \boldsymbol{V}) = 0, \tag{1}$$

$$\frac{\partial}{\partial t}(\rho \boldsymbol{v}) + \nabla \cdot \left(\rho \boldsymbol{V}\boldsymbol{V} + p\boldsymbol{I} - \frac{\boldsymbol{B}\boldsymbol{B}}{4\pi} + \frac{\boldsymbol{B}^2}{8\pi}\boldsymbol{I} \right) - \rho \boldsymbol{g} = 0, \tag{2}$$

$$\frac{\partial}{\partial t}\left(\rho U + \frac{1}{2}\rho \boldsymbol{V}^2 + \frac{\boldsymbol{B}^2}{8\pi} \right) + \nabla \cdot \left[(\rho U + p + \frac{1}{2}\rho \boldsymbol{V}^2)\boldsymbol{V} + \frac{c}{4\pi}\boldsymbol{E} \times \boldsymbol{B} \right] - \rho \boldsymbol{g} \cdot \boldsymbol{V} = 0, \tag{3}$$

$$\frac{\partial \boldsymbol{B}}{\partial t} - \nabla \times (\boldsymbol{V} \times \boldsymbol{B}) = 0, \tag{4}$$

and

$$U = \frac{1}{\gamma - 1}\frac{p}{\rho}, \tag{5}$$

$$\boldsymbol{E} = -\frac{1}{c}\boldsymbol{V} \times \boldsymbol{B}, \tag{6}$$

where ρ is the density, $\boldsymbol{V} = (V_x, V_y, V_z)$ is the velocity vector, p is the thermal pressure, t is the time, $\boldsymbol{g} = (0, 0, -g)$ is the gravitational acceleration, c is the light velocity, $\boldsymbol{I}$ is the unit tensor, U is the internal energy, $\boldsymbol{B} = (B_x, B_y, B_z)$ is the magnetic vector, $\boldsymbol{E}$ is the electric field and the other symbols have their usual meanings.

2.2. Initial Condition and Parameters

In the simulations the units of length, velocity, and time are H,C_s and $H/C_s \equiv \tau$, respectively, where C_s and H are the sound speed and pressure scale height in the photosphere/chromosphere. It is to be noted that the photospheric temperature T_{ph} can be calculated from C_s, since $T_{ph} = \mu C_s^2/(\gamma R_g)$, where μ and R_g are the mean molecular weight and gas constant, respectively. Therefore we need not specify the value of T_{ph} explicitly. The units for gas pressure, density, and magnetic field strength are $p_0 \equiv \rho_0 C_s^2$, ρ_0 (the initial density at the base of the gas layer, $z = z_{min}$), and $B_0 \equiv (\sqrt{\rho_0 C_s^2})$, respectively. When the numerical results are compared with observations, we use $H = 200$km, $C_s = 10$km s^{-1}, and $\tau = H/C_s = 20$s, which are typical values for the solar photosphere and chromosphere. In this case, $B_0 \simeq 500$G if it is assumed $\rho_0 = 2.5 \times 10^{-7}$g cm^{-3}. However, it is noted that our results are valid for any values of C_s, H, ρ_0, because our

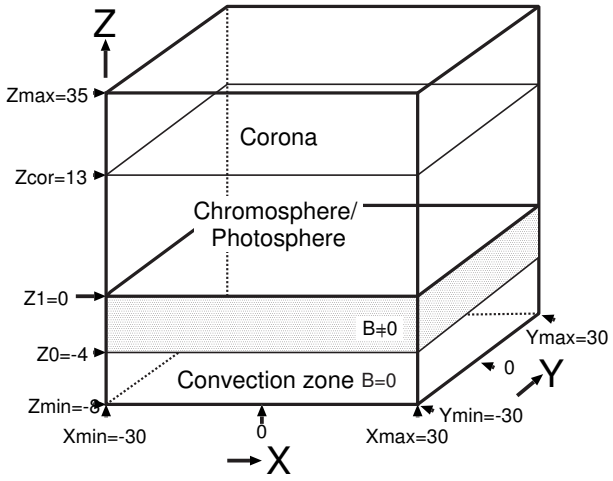

Fig. 1. Convection zone and photosphere (and chromosphere, corona) adiabatic temperature gradient a=0.0 density, pressure, magnetic pressure are a static pressure balance in initial perturbation: local and random velocity (V_z) x, y periodic boundary, z_{min} rigid boundary, z_{max} free boundary

model is non-dimensional and scale-free.

2.3. Unperturbed State (Initial Conditions)

We consider that the initial state is in magnetohydrostatic equilibrium. The gas layer is initially composed of three regions (see figure 1): a convectively stable layer represents a very simplified model of the solar photosphere/chromosphere and corona. The temperature is nearly constant in the upper hot layer (corona) and in the lower cold layer (photosphere/chromosphere). We take the height $z = 0$ to be the base height of the photosphere, and the initial distribution of temperature in the photosphere/chromosphere and the corona is

$$T(z) = T_{ph} + \frac{1}{2}(T_{cor} - T_{ph}) \left[\tanh\left(\frac{z - z_{cor}}{w_{tr}} \right) + 1 \right], \quad (7)$$

where T_{cor} and T_{ph} are the respective temperatures in the corona and in the photosphere/chromosphere respectively, z_{cor} is the height of the base of the corona, and w_{tr} is the temperature scale height in the transition region. We take $w_{tr} = 0.6H$ and $z_{cor} = 13H$ in all our calculations.

We assume that the magnetic field is initially horizontal, $\boldsymbol{B} = (B_x(z), B_y(z), 0)$, and is localized under the photosphere. The initial density and pressure distributions are calculated numerically using the equation of magnetohydrostatic pressure balance:

$$\frac{d}{dz}\left[p + \frac{B_x^2(z) + B_y^2(z)}{8\pi} \right] + \rho g = 0, \quad (8)$$

where

$$B_x(z) = \left(\sqrt{\frac{8\pi p(z)}{(z)}} \right) \cos\theta(z), \quad (9)$$

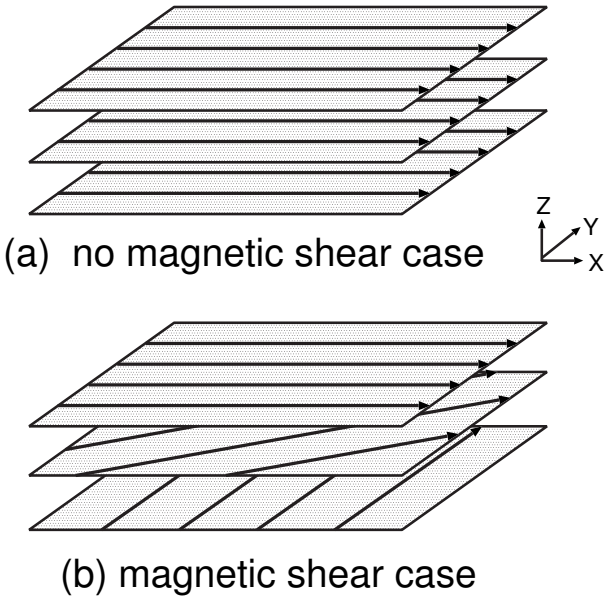

Fig. 2. Degree of magnetic shear in the magnetic sheet; (a) is for the case no magnetic shear and (b) is for the case with magnetic shear. In the upper magnetic layer magnetic direction is parallel to x direction for both cases. In the lower magnetic layer it is parallel to y direction ($\theta = 1/2\pi$) for the case with shear.

$$B_y(z) = \left(\sqrt{\frac{8\pi p(z)}{(z)}} \right) \sin\theta(z), \quad (10)$$

and the plasma is the ratio of gas pressure to magnetic pressure, with

$$(z) = {}_*/f(z) \quad (11)$$

where

$$f(z) = \left[1 + \tanh\left(\frac{z - z_0}{w_0}\right)\right]\left[1 - \tanh\left(\frac{z - z_1}{w_1}\right)\right]/4. \quad (12)$$

Here ${}_*$ is at the center of the magnetic flux sheet, z_0 and $z_1 = z_0 + D$ are the heights of the lower and upper boundaries of the magnetic flux sheet, and D is the vertical thickness of the magnetic flux sheet. We use $D = 4H \simeq 800$km, and $w_0 = w_1 = 0.5H$, for all of our calculations and take to be nearly constant inside the flux sheet($z_0 \le z \le z_1$). The magnetic field direction $\theta(z)$ is given by

$$\theta(z) = \theta_{00}\pi(z_1 - z)/D, \quad (13)$$

when $z_0 \le z \le z_1$, $\theta_{00} \ge \theta(z) \ge 0$. Figure 2b shows that the magnetic field lines at each height have different horizontal directions.

The free parameters are ${}_*, z_{min}$ (depth of the convection zone), and z_0 (base height of the flux sheet). We will use the case with $= 1$, $z_{min} = -8H \simeq -1200$ km and $z_0 = -4H \simeq -800$ km. Although these values are not realistic for the actual solar convection zone (e.g., Spruit 1974;

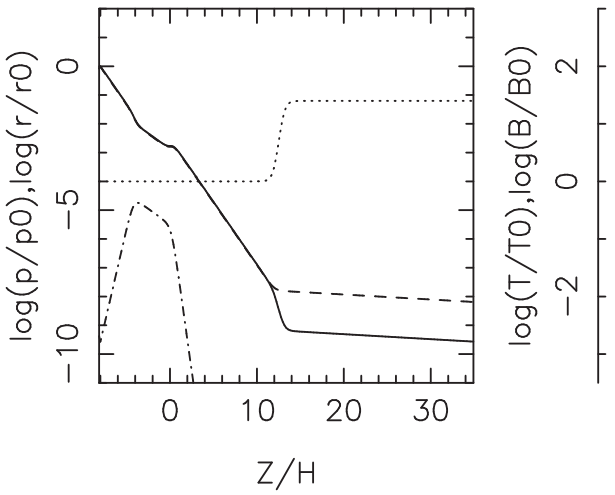

Fig. 3. One-dimensional (z-) distribution of the initial density (solid curve), pressure (dashed curve), magnetic field strength (dash-dotted curve), and temperature (dotted curve). ρ_0, p_0, T_0, B_0 denote the initial density, pressure, temperature, and magnetic field strength at $z = z_{min}$ ($z = -8H$), respectively.

Spruit et al. 1990), they are acceptable for our first attempt to study the fundamental nonlinear interaction between the magnetic field and convection just below the photosphere.

The initial temperature (T), density (ρ), gas pressure (p), and magnetic field strength ($|\boldsymbol{B}|$) distributions for our base model ($z_{min} = 8, z_0 = -4H$, $_* = 1$) are shown in figure 3.

2.4. Boundary Conditions

We assumed a rigid conditional wall at $z = z_{min}$ and $z = z_{max}$, and periodic boundaries at $x = x_{min}$, $y = y_{min}$ and $x = x_{max}$, $y = y_{max}$, respectively. The rigid wall is the simplest and most reliable condition to implement of $z = z_{min}$ in the high-energy density region of the convection zone. The difficulties are particularly acute here, since the density ratio between the convection zone and the corona is 10^{-7}, so that small errors generated at the free boundary at $z = z_{min}$ are enormously amplified by the steep density gradient in the photosphere and chromosphere as they propagate from the convection zone into the corona. The effect of the rigid boundary at $z = z_{max}$ is small, since the energy density is smallest in the computational box.

2.5. Numerical Method

Non-dimensional MHD equations (1)-(6) are solved numerically by using a modified Lax-Wendroff scheme (Rubin and Burstein 1967) with artificial viscosity (Ritchmyer & Morton 1967), as in previous studies (e.g., Shibata 1983; Matsumoto et al. 1988; Shibata et al. 1989a, 1989b, 1990b; Nozawa et al. 1992; Matsumoto et al. 1993, 1998).

The magnetohydrostatic gas layer shown above is unstable for the interchange and Parker instabilities. In order to start the instability, small velocity perturbations of the form

$$V_z = f(z) A C_s \cos\left[\frac{2\pi x}{\lambda_x}\right] \cos\left[\frac{2\pi y}{\lambda_y}\right] \tag{14}$$

are given initially within the finite horizontal domain ($|x, y| \le \lambda/2$), where λ is the wavelength of the small velocity perturbations. A typical case is $\lambda_x = \lambda_y (k_y/k_x = 1)$. C_s is the sound speed in the photosphere, and A is the maximum value of V_z/C_s in the initial perturbation. In the two-dimensional case (model 1), a small velocity perturbation is used of the form

$$V_x = f(z) A C_s \sin\left[\frac{2\pi x}{\lambda}\right]. \tag{15}$$

Although the distribution of the velocity given by equation (14) is not exactly equal to an eigenfunction, the growth rate of the perturbation in the linear regime agrees well with that obtained from the exact linear analysis, as will be discussed in Appendix (see also Matsumoto et al. 1988; Shibata et al. 1989a).

The mesh size is $\Delta z_0 = 0.15H$ for $z \le z_{cor}$, and this slowly increases up to $\Delta z_{max} = 0.375H = T_{cor}/10 \times \Delta z_0$ for $z \ge z_{cor}$, and $\Delta x, \Delta y = 0.2$. The total number of mesh points is $N_x \times N_y \times N_z = 300 \times 300 \times 203$, and the total area is $[x_{max} \times y_{max} \times (z_{max} - z_{min})] = (60H \times 60H \times 43H)$. The parameters of the models studies here are summarized in Table 1.

3. Nonlinear Simulation results

3.1. The case of 2D (model 1)

Let us first discuss the typical nonlinear evolution of the Parker instability in the 2D case. Figures 4 and 5 show the typical results for the no shear mode.

All results agree with those of Shibata et al. (1989a) except for the time sequence; the time evolution of the emerging flux loop is slow compared with Shibata et al. (1989a,1989b), because the perturbation amplitude A is taken to be 10^{-3}. We can see a self-similar evolution for the density (figure 5a) and magnetic field strength (figure 5d),

$$\rho \propto z^{-4}, \quad B \propto z^{-1}. \tag{16}$$

In particular the plasma decreases to less than 0.1, which indicates that the magnetic pressure is dominant against gas pressure and the magnetic loop continues to rise up (figure 5f). The magnetic pressure dominance leads to forming the current-free magnetic loop.

3.2. The case of no magnetic shear with a localized perturbation (model 2)

Let us now discuss the 3D cases. Figures 6, 7, and 8 show typical results in the no shear mode. Figure 8c indicates that the magnetic field in the y-direction emerges from the narrow region and expands horizontally in the photosphere. The 3D display in figures 8a,b show that the magnetic field lines become almost vertical in the region where the magnetic field is concentrated.

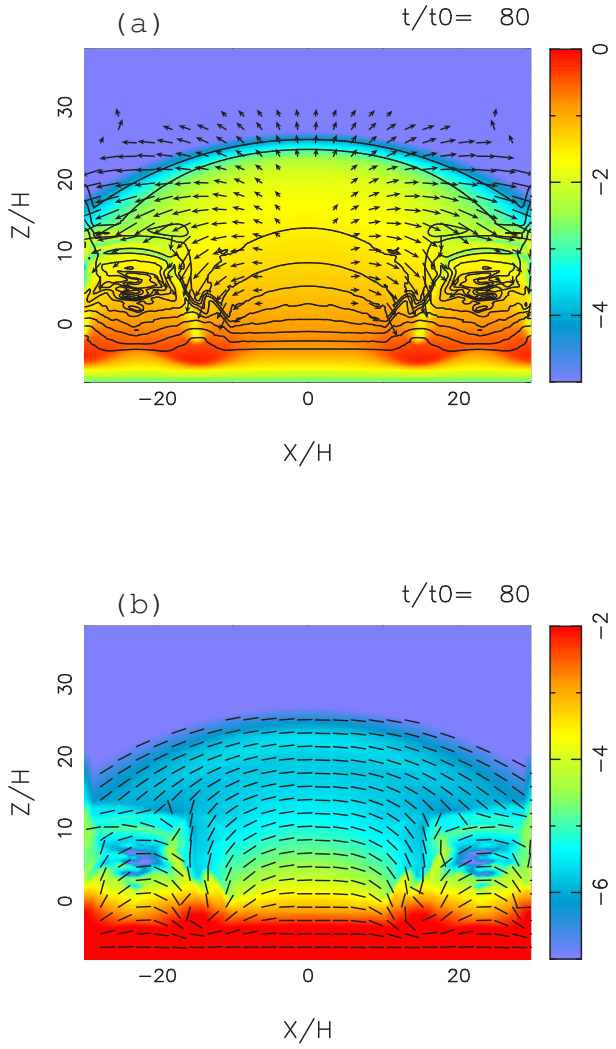

Fig. 4. 2D distribution of (a) magnetic field strength $|B| = \sqrt{B_x^2 + B_z^2}$ (gray scale colors), velocity field (vectors), density (contours), (b) magnetic field lines (lines) and density (gray scale colors), at $t/\tau_0 = 80$ for 2D case (model 1). The velocity length $1H$ is $1C_s$ (sound velocity).

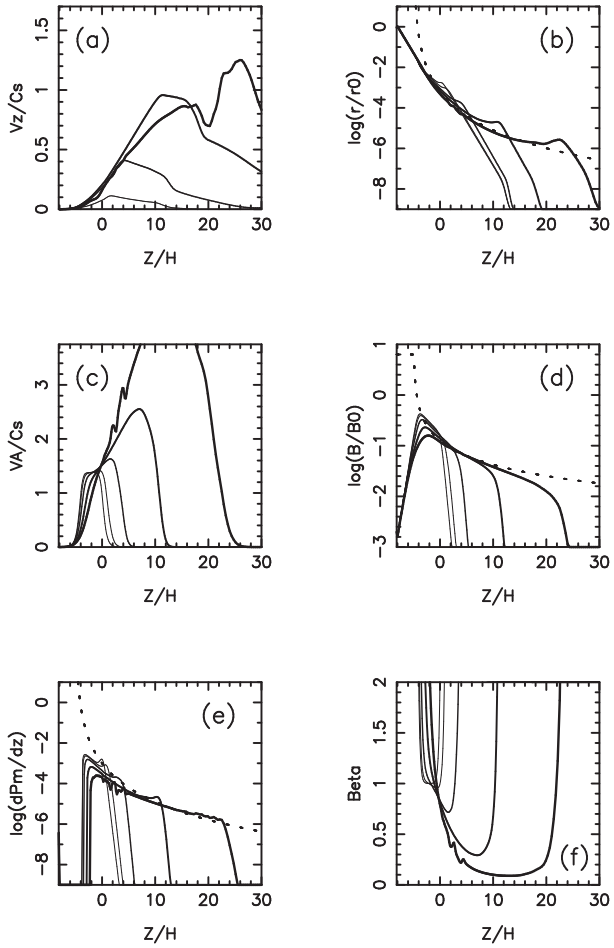

Fig. 5. Distribution in z of (a) the vertical component velocity (V_z), (b) the density($\log\rho$),(c) the local Alfve'n speed (V_A), (d) the horizontal component of the magnetic field ($\log B$), (e) the magnetic pressure ($\log(\Delta P_m/\Delta z)$), and (f) plasma β (gas pressure/magnetic pressure) at $x = 0$ (middle of the rising loop) for model 1 (the case shown in figure 4) at $t/\tau_0 = 0, 50, 60, 70, 80$.

In the upper photosphere the magnetic field is parallel to the photospheric plane, and expands horizontally. Since the scale height of the photosphere is smaller than the thickness of a magnetic sheet, the gas pressure outside of the sheet decreases rapidly. Hence, when the magnetic field emerges a little into the photosphere, magnetic flux expands horizontally until the magnetic pressure of the sheet balances with the surrounding gas pressure.

The velocity vectors also show that plasma expands in the horizontal direction more than the vertical direction (see figures 8b,c,d). This result implies that the rise of the magnetic loop is stopped at lower heights ($< 10H$) and the distribution of magnetic pressure is in a new state of magnetohydrostatic equilibrium.

Although in figure 8a the characteristic wavelength in the x-direction is comparatively long $27-32H$, the characteristic wavelength in the y-direction is short $2-6H$. But at $z = 7H$ (see figure 8b) the characteristic wavelength in both the x and y-directions increase to $35-40H$, because of the inverse cascade effect (Hachisu et al. 1992).

In figure 8a at $t/\tau_0 = 50$ the top of the magnetic loop reached $z/H = 14H$. In the last stage the magnetic loop does not rise any more. Figures 8b,d,e show the distributions of density, magnetic field strength and magnetic pressure which are approximated by

$$B \propto \exp\Big(-\frac{\Delta z}{H_B}\Big), \quad \rho \propto \exp\Big(-\frac{\Delta z}{H_\rho}\Big), \quad P_m \propto \exp\Big(-\frac{\Delta z}{H_{Pm}}\Big)$$

with H_B $4, H_\rho$ $2, H_{Pm}$ 2. What is the physical meaning of these distributions? They are similar to typical distributions of the magnetic field and plasma in magnetohydrostatic equilibrium with uniform temperature and constant plasma , when the magnetic field is horizontal. In fact, an exact equilibrium solution predicts $H_\rho = (1+\frac{1}{\beta})H$, $H_{Pm} = H_p = H_\rho$. In our simulation results, $= 0.7-1.0$ (see figure 8f), so that we have H_ρ $2-2.3$, which is

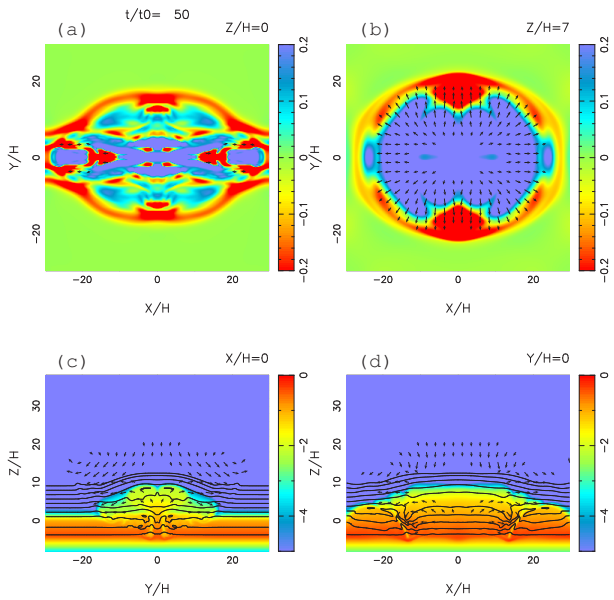

Fig. 6. Nonlinear simulation results for the case of no magnetic shear, where a localized perturbation is initially assumed (model 2). (a) shows distribution of V_z on the photosphere surface ($z = 0H$). (b) shows velocity distribution in the upper photosphere ($z = 7H$). Magnetic field(color), velocity field(vector), density(contour line) on y-z surface for (c) and on x-y surface for (d) are shown.

consistent with direct simulation results (H_ρ 2). Other relations H_ρ H_{Pm} $H_B/2$ are also consistent with magnetohydrostatic equilibrium theory.

Note that the plasma $=0.7-1.0$ in the rising magnetic loop is larger than that in 2D (0.1). This is because magnetic flux rapidly expands in the horizontal direction in the photosphere, so that the magnetic field becomes weak. Hence the magnetic flux cannot expand into the corona, and instead tends to be in magnetohydrostatic equilibrium in the photosphere and chromosphere.

3.3. The case of magnetic shear with a localized perturbation (model 3)

Figures 9, 10, and 11 show the results in the 3D calculation for the shear mode.

In figure 9a and 10a, the loop which passes the origin $(X = 0, Y = 0)$ emerges at 45° angle to the x-direction, while in the case of the no shear the loop is parallel to the x-direction. This is because the magnetic sheet at the depth where the field line is parallel to the 45 degrees rises up in the photosphere at $t/\tau_0 = 50$. In the last stage of the calculation after $t/\tau_0 = 50$, a deeper magnetic sheet rises up and it becomes a loop with an angle greater than the 45 degrees.

Figure 9c indicates that the area where the magnetic sheet rises up in the photosphere is larger than that of the no shear. In the shear case, the velocity vectors show that the plasma expand in the horizontal direction more than the vertical direction (see figures 9b,c,d), and the magnetic field expands at middle heights $(6-12H)$. Figure 11a shows that the characteristic wavelength in the x-direction is comparatively long $13H$ and the characteristic wavelength in the 45°-direction is somewhat short $4-8H$.

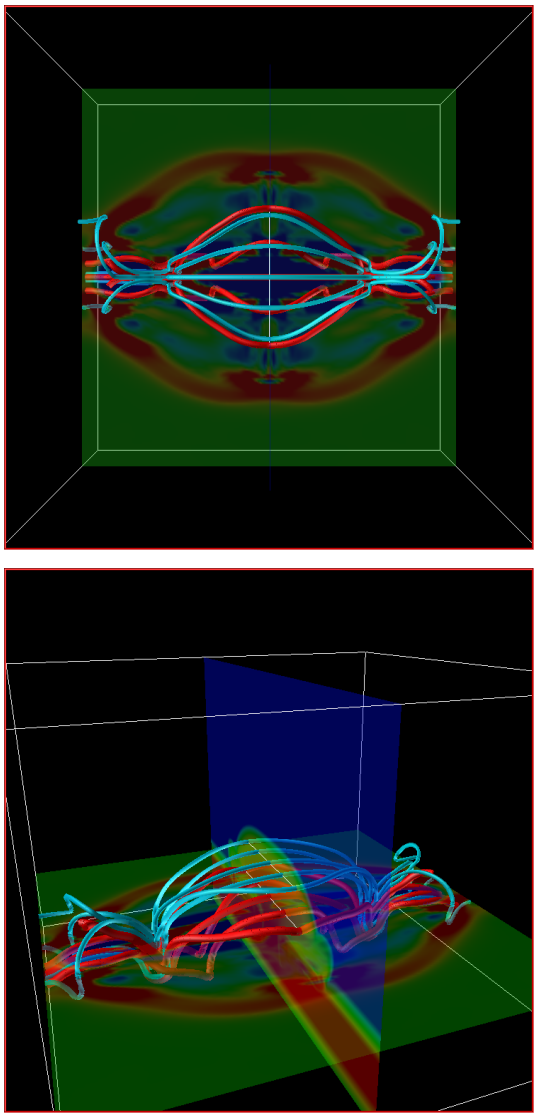

Fig. 7. Perspective view of the magnetic field at the epochs $t/\tau_0 = 55$ for the case of no magnetic shear, where a sinusoidal perturbation is initially assumed(model 2).

Similarly to the no shear case, the plasma density and magnetic field strength distribution in the shear mode case are also approximated by exponential ones (eq.17) with H_ρ $2, H_B$ 4 (see figures 11b,d) and the plasma 1 in the magnetic loop (see figure 11f).

3.4. The case of a random perturbation (model 4 and model 5)

Figure 12 shows the results in the case of random initial perturbation for both no shear and shear modes. In the early stage ($\simeq t/\tau_0 = 30$ (see figures 12a,d)) the characteristic wavelength in the y-direction is small and equal to $\lambda = 3.5H$($60H/17$). Subsequently the wavelength increases to $\lambda = 4.6H$($60H/13$) at $t/\tau_0 = 40$ (see figures 12b,e), and $\lambda = 5.5H$($60H/11$) at $t/\tau_0 = 50$ (see figures

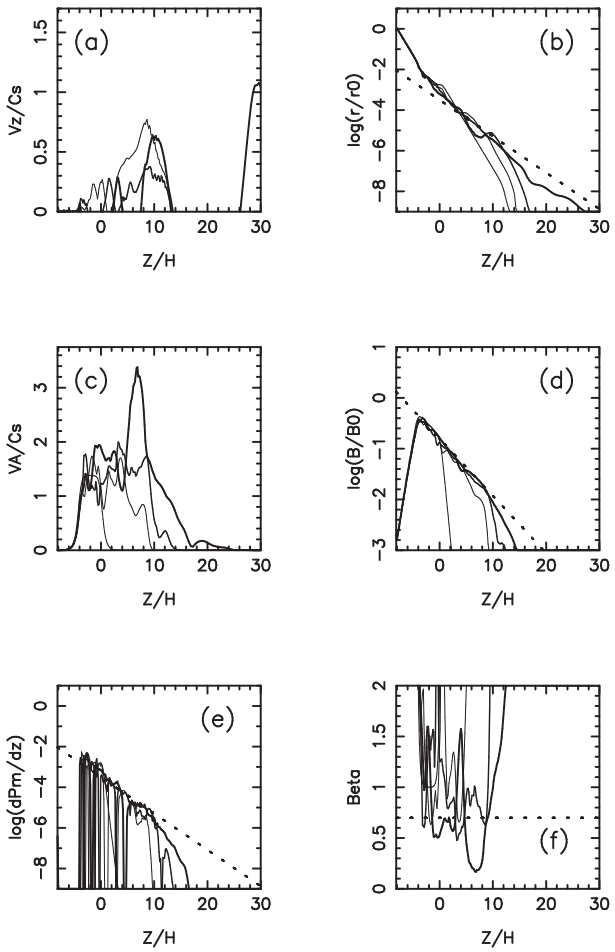

Fig. 8. Distribution in z at $(x,y)=(0,0)$ (middle of the rising loop) for model 2 (the case of no shear mode) shown in figure 8 at $t/\tau_0=0,50,60,70$ in $x,y=10H$, and other remarks are the same as in figure 5. The dashed lines in (b),(d) and (e) indicate the lines of $\rho\propto\exp(-\Delta z/H_\rho)$ with $H_\rho=2.0$, $B\propto\exp(-\Delta z/H_B)$ with $H_m=4.0$, and $P_m\propto\exp(-\Delta z/H_{P_m})$ with $H_{P_m}=2.0$. In (e) the dashed lines is $beta=0.7$.

12c,f). In figure 13b,d at $t/\tau_0=50$ the magnetic loop rises at $z/H=19H$ in the no shear case and at $z/H=13H$ in the shear case. The distributions of plasma density and magnetic field are basically the same as those in previous 3D cases (eq. 17).

3.5. The case of a periodic perturbation (model 6 and model 7)

Figure 14 shows two cases of simulation results in which the initial perturbation is periodic in the $kH=0.7,\lambda_x,\lambda_y=12.6H,k_x=k_y=0.5,k_y/k_x=1$ no shear and shear modes case. In both cases, the distributions of the density, pressure and magnetic field do not correspond to those of the magnetohydrostatic equilibrium but of the potential field (eq. 16). That is the expansion of the magnetic loop dose rising to corona, and the physical processes are basically the same as those in the 2D case.

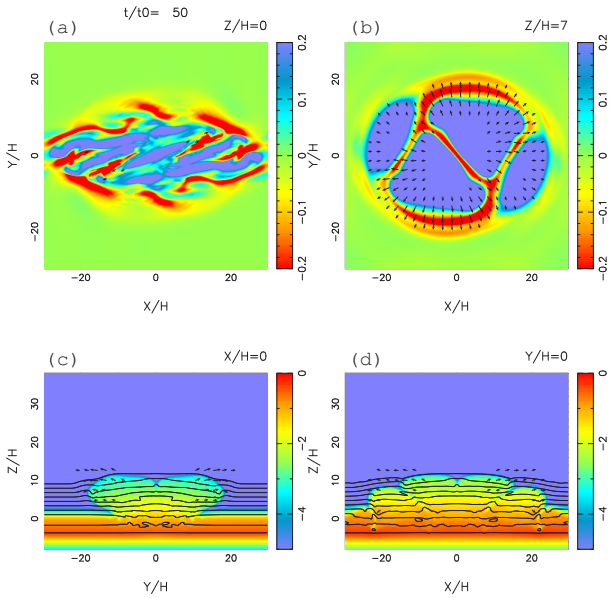

Fig. 9. Nonlinear simulation results for the case of magnetic shear, where a sinusoidal perturbation is initially assumed(model 3), and other remarks are the same as in figure 7. In (e) the dashed lines is $beta=0.9$.

3.6. Loop height for different shear case

Figures 15 and 16 show the loop height in each simulation result at $t/\tau_0=55$. When $k_y/k_x<1$, it is easy to cause the Parker instability, so each loop height goes up comparatively high, to $15-24H$. On the other hand, in the $k_y/k_x>1$ case the interchange instability occurs easily, and the height monotonously decreases when k_y is larger.

When $k_y/k_x<1$, h/L_x and h/L_y are $0.3-0.5$, the loop becomes horizontally expanded. Hence, when $k_y/k_x>1$, the loop height increases with shear angle θ_{00} (eq. 13), and the height increases when k_y is larger. This is basically due to the stabilizing effect of magnetic shear in the interchange model.

4. Summary and Discussion

4.1. Summary

Three dimensional simulations show the followings:

- When the magnetic field emerges into the photosphere with the localized and random initial perturbation, the flux expands horizontally and does not go upward. At that time, the distributions of magnetic field strength, density, and pressure are written as $\exp(-\Delta z/H_{(m,\rho,p)})$ as in magnetohydrostatic equilibrium, and the plasma of magnetic loop is $0.3-1.3$ (magnetic field strength is weak).
- When a periodic perturbation is initially assumed, the emerging flux rises up to the corona and the magnetic field expands like a potential field as in two dimensional typical case. The plasma of magnetic loop is lower ($0.01-0.1$) than that of three

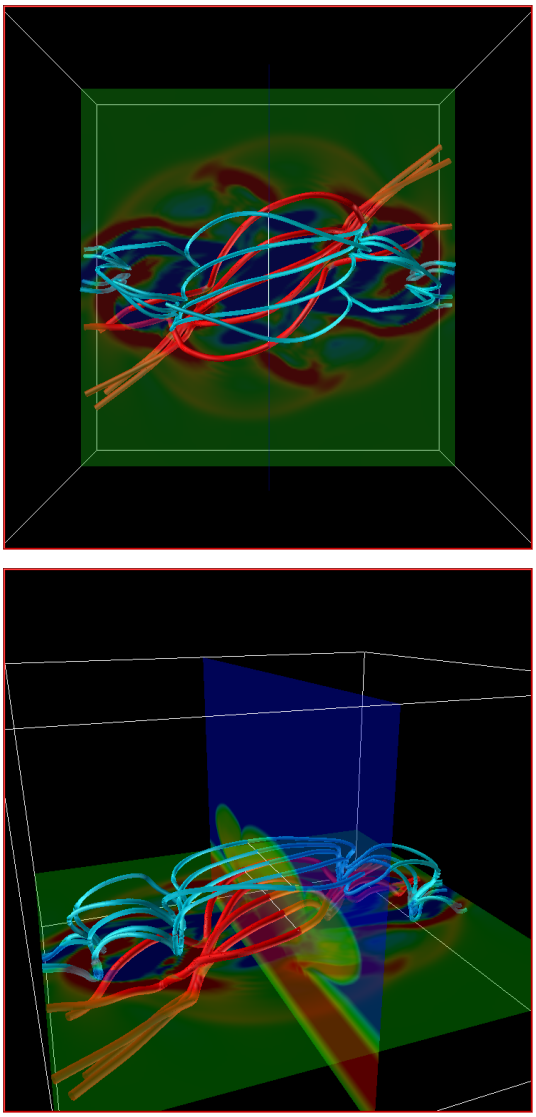

Fig. 10. Perspective view of the magnetic field at the epochs $t/\tau_0 = 55$ for the case of magnetic shear, where a sinusoidal perturbation is initially assumed (model 3).

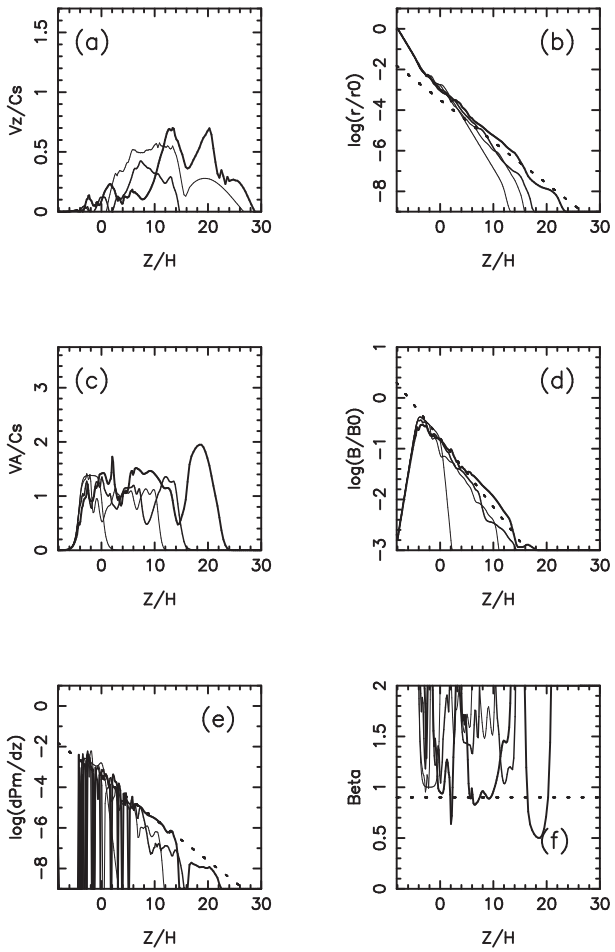

Fig. 11. Distribution in z at $(x, y) = (0, 0)$ (middle of the rising loop) for model 3 (the case of shear mode) shown in figure 9 at $t/\tau_0 = 0, 50, 60, 70$ in $x, y = 10H$, and other remarks are the same as in figure 5.

dimensional case.

- When there is no magnetic shear, magnetic flux cannot rise as a whole (i.e., as a global or thick magnetic loop), but rise as fragmented flux tubes because of interchange instability. In this case, the flux tube expands significantly in a horizontal direction, so that the average magnetic pressure decreases very much and hence the tube soon stops at low height. However, when there is magnetic shear, the interchange mode is stabilized (see Appendix for a linear stability analysis), so that the tube can rise as a whole and hence the height of the loop becomes higher (see Fig. 16). For the same reason, the loop height increases with shear angle or k_y.

4.2. Discussion

Shibata et al. (1989a) and other studies show that in two dimensional calculations the emerging magnetic flux rises into the corona, with the density given by $\rho \propto z^{-4}$ and the magnetic field given by $B_x \propto z^{-1}$, due to a potential magnetic field. In the momentum equation the gravity term $\rho g \quad z^{-4}$ is smaller than the magnetic term B^2/dz z^{-3}, and therefore the expansion of the magnetic loops is not stopped in the two dimensional model.

When a periodic perturbation is initially assumed, the emerging flux rises up to the corona and the magnetic field expands like a potential field. This special case is similar to Model 10 of Matsumoto et al. (1993) where the initially straight magnetic tubes are placed side by side. Because the emergence of each tube occurs at the same time, the expansions are blocked in the horizontal direction by each other and so they rise in the vertical direction. In this case the emerging loop structure is similar to the two dimensional case(see figure 17a).

This result explains why a twisted magnetic tube rises up into corona in the cases of Magara, Longcope (2003)

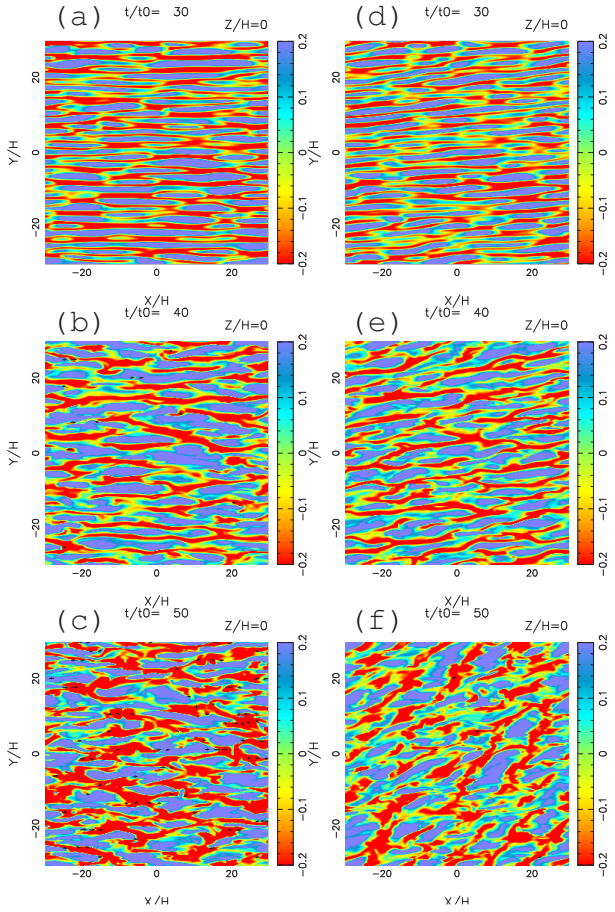

Fig. 12. Nonlinear simulation results for the case of no magnetic shear mode (left; a,b,c; model 4) and of magnetic shear mode (right; d,e,f; model 5), where a random noise perturbation is initially assumed. These figures show distribution of V_z on photosphere surface ($z = 0H$) at $t/\tau_0 = 30, 40, 50$.

and Fan, Gibson (2004). The tube is twisted very strongly. Because the interchange instability occurs on the surface of the tube, the flux tube expands up both horizontally and vertically. The horizontal expansion is blocked on both sides by other emerging flux. However, after the photosphere is full of magnetic field, the flux emerges from the upper photosphere to the corona in realistic simulation of the solar atmosphere (see figures 13b). The critical wave length λ_c in the photosphere is estimated:

$$\lambda_c \quad 2\pi H(1+\frac{1}{}) \tag{18}$$

When $= 0.5$, we find $\lambda_c \quad 18H$. In fact, figure 13b shows that the wave length of emerging flux into corona is roughly $18H$ in agreement with the above estimate. As a localized perturbation is initially assumed, the emerging flux expands in the photosphere (see figure 17b). When random perturbation is also initially assumed, each loop top of emerging flux is different and magnetic loop expands horizontally like the growth of localized perturbation loop (see figure 17c).

In figure 18a at $t/\tau_0 = 35 - 40$, the expansion velocity

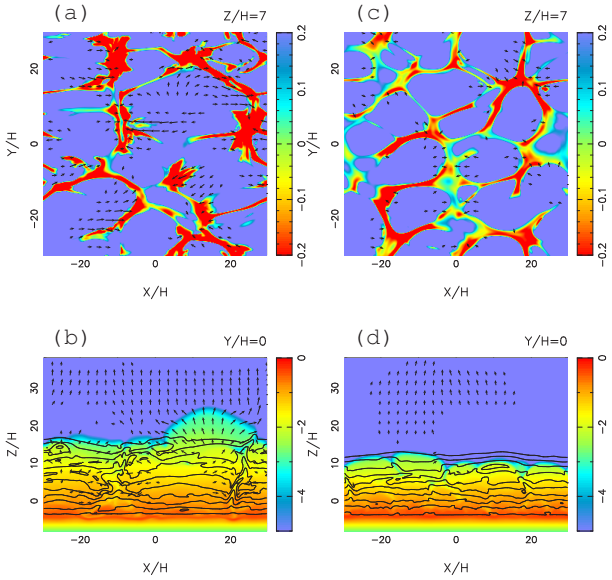

Fig. 13. Nonlinear simulation results for the case of no magnetic shear mode (left) and of magnetic shear mode (right), where a random noise perturbation is initially assumed (model 4 and model 5). Upper figures show distribution of V_z on the upper photosphere surface ($z = 7H$) and lower figures show magnetic field(color), velocity field (vector), density (contour line) on $x - y$ surface.

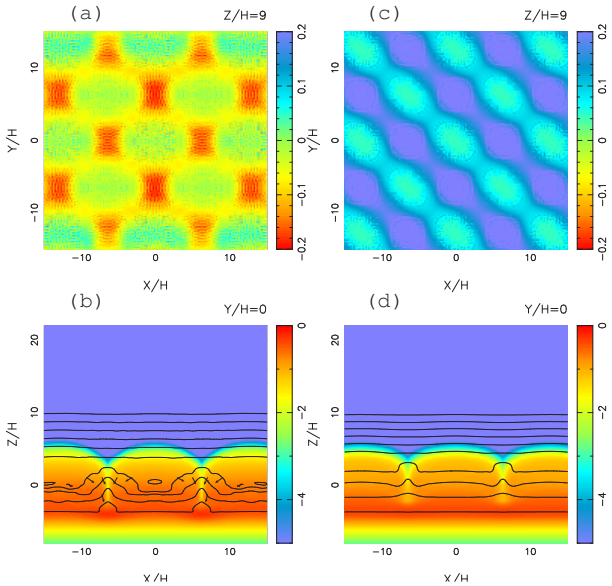

Fig. 14. Nonlinear simulation results for the case of no magnetic shear mode (left; model 4) and magnetic shear mode (right; model 5), where a periodic perturbation is initially assumed, and other remarks are the same as in figure 12.

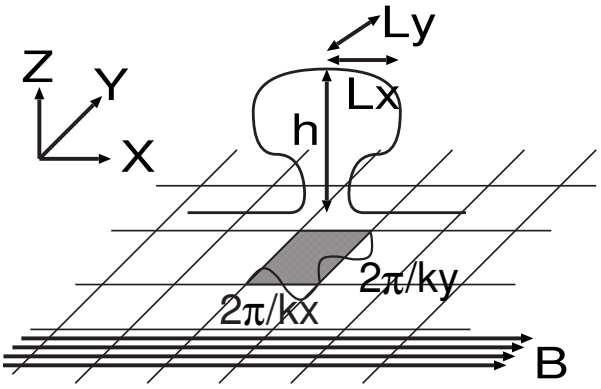

Fig. 15. Definition of h, L_x, L_y in a loop.

in the horizontal direction is $1.0 - 1.5C_s$. This velocity is estimated by assuming that the kinetic energy is equal to the magnetic energy, $\rho v^2 \quad B^2/(8\pi)$. Where $\rho \quad p/C_s^2$, $v^2 \quad B^2/(8\pi p/C_s^2) = C_s^2/$. If $\quad = 1$, $v \quad 1C_s$ =10km/s. Although this velocity is large enough compared to the observed typical value the photosphere, the expansion timescale is very short ($\simeq 5$ minutes, see figure 18b) and the size is small ($\simeq 4000$km). Therefore such phenomena may be observed with high resolution observed by La Palma, Swedish Vacuum Solar Telescope (De Pontieu et al. 2004), but future observations such as Solar-B will reveal these detailed features of emerging flux.

The author would like to thank Prof. K. Shibata and all the members of Kwasan Observatory, Kyoto University for fruitful discussions and various help. He is also grateful to Dr. D. Brooks for his careful reading of the manuscript and many valuable comments. This work was carried out by the joint research program of the Solar-Terrestrial Environment Laboratory, Nagoya University. This work was supported in part by the JSPS Japan-UK Cooperation Science Program (principal investigators: K. Shibata and N. O. Weiss).

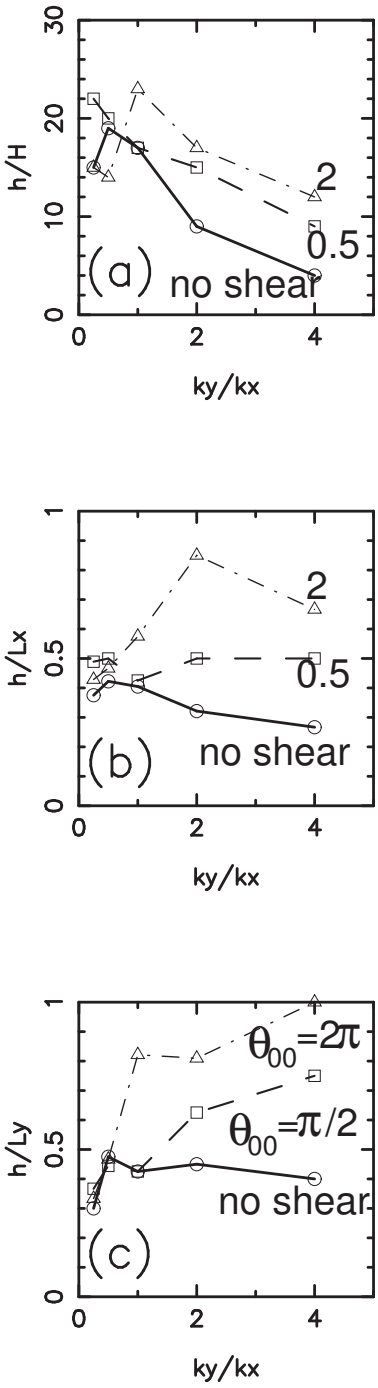

Fig. 16. The normalized loop height ($h/H, h/L_x, h/L_y$), as a function of k_y/k_x at $t/\tau_0 = 55$ in the case of the localized perturbation. Numbers indicate the shear angle θ_{00}(radian). Here, h is the height of emerging flux loop, L_x is the half length of the loop and L_y is the width of the loop (see figure 15).

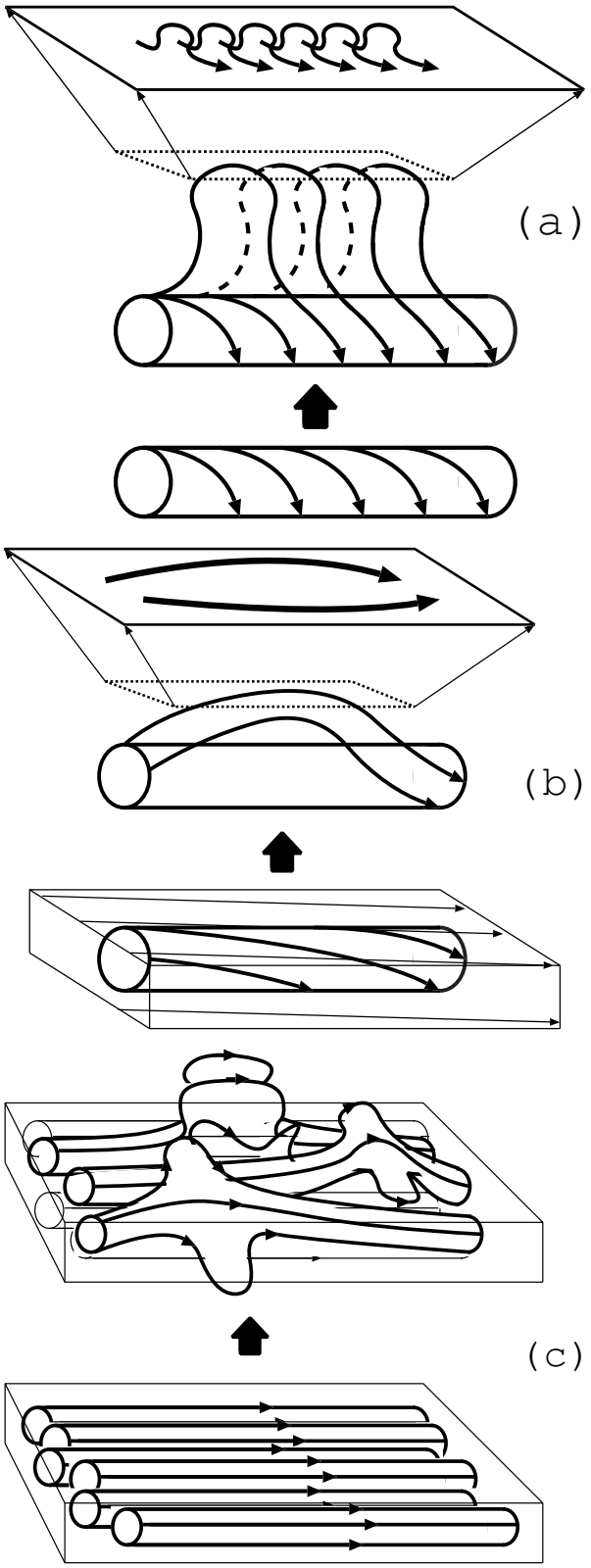

Fig. 17. Schematic pictures of emergence in (a) strong twisted flux tube, (b) weak twisted flux tube or magnetic flux sheet, and (c) random perturbation with no magnetic shear.

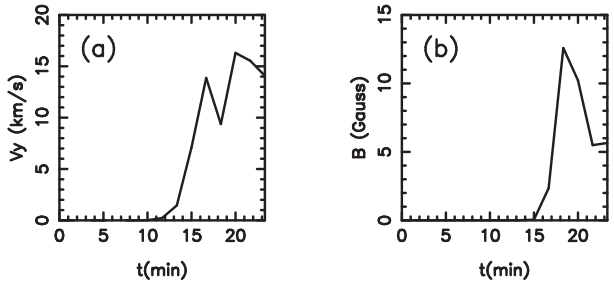

Fig. 18. Time evolution of the y component of the velocity and magnetic strength at $x = 0H, y = 10H, z = 5H$, for the case shown in model 2.

Table.1 Models And Parameters

model	2D or 3D	$k_x HorkH, \lambda$	shear	ky:kx
1	2D	0.31,20H	0.0	—
2	3D	0.5,12.6H	0.0	1:1
3	3D	0.5,12.6H	0.5π	1:1
4	3D	random	0.0	1:1
5	3D	random	0.5π	1:1
6	3D	0.5,12.6H,periodic	0.0	1:1
7	3D	0.5,12.6H,periodic	0.5π	1:1
8	3D	0.5,12.6H	2.0π	1:1
2a	3D	0.5,12.6H	0.0	1:8
2b	3D	0.5,12.6H	0.0	1:4
2c	3D	0.5,12.6H	0.0	1:2
2d	3D	0.5,12.6H	0.0	2:1
2e	3D	0.5,12.6H	0.0	4:1
2f	3D	0.5,12.6H	0.0	8:1
3a	3D	0.5,12.6H	0.5π	1:8
3b	3D	0.5,12.6H	0.5π	1:4
3c	3D	0.5,12.6H	0.5π	1:2
3d	3D	0.5,12.6H	0.5π	2:1
3e	3D	0.5,12.6H	0.5π	4:1
3f	3D	0.5,12.6H	0.5π	8:1
8a	3D	0.5,12.6H	2.0π	1:8
8b	3D	0.5,12.6H	2.0π	1:4
8c	3D	0.5,12.6H	2.0π	1:2
8d	3D	0.5,12.6H	2.0π	2:1
8e	3D	0.5,12.6H	2.0π	4:1
8f	3D	0.5,12.6H	2.0π	8:1

Appendix 1. Linear Stability Theory and Comparison with Nonlinear Simulation

A.1.1. Linear Theory

In order to study the main characteristics of the linear instability of the magnetic flux sheet with magnetic shear, we analyze the linear stability of the flux sheet with a normal-mode method similar to that of Horiuchi et al. (1988). We consider the growth of a small perturbation which has a functional form $\delta W \propto \exp(i\omega t + ik_x x + ik_y y)$, where W is the physical quantity $(\rho, p, v, \boldsymbol{B})$, and δW is its perturbation. The linearized equations are the same as those in Horiuchi et al. (1988) and Nozawa et al. (1992), and the eigenvalues (ω) and eigenfunction are calculated

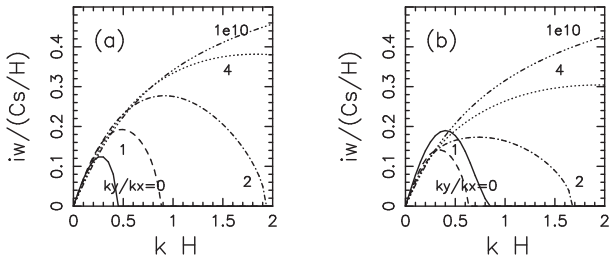

Fig. 19. Normalized growth rate (in units of C_s/H) as a function of k for $k_y/k_x = 0, 1, 2, 4, \infty$(1.e10) for (a) the case of no magnetic shear mode and (b) the case of magnetic shear mode. $\beta_* = 1.0, \gamma = 1.05$ are assumed. $kH = \sqrt{k_x^2 + k_y^2}H$

.

numerically.

Figure A1 shows the growth rates $i\omega$ as a function of horizontal wave number $kH = H\sqrt{k_x^2 + k_y^2}$ for two cases, (a) no shear mode, and (b) shear mode, when $_* = 1, \gamma = 1.05, D = 4H, z_{min} = -8, z_0 = -4H, z_{cor} = 13H$ and $T_{cor}/T_{ph} = 25$.

The numbers attached to each curve indicate the ratio k_y/k_x. When the wavenumber along the field line (k_x) is fixed, the growth rate increases with perpendicular wavenumber k_y. Thus a perturbation with a shorter wavelength perpendicular to the magnetic field line grows faster than perturbations with longer-wavelengths.

The linear growth rate of our non-sinusoidal perturbations (14) is the same as that of sinusoidal (single plane wave) in the shear mode case because the non-sinusoidal perturbation can be decomposed into two plane wave perturbations whose wave vectors are (k_x, k_y) and $(k_x, -k_y)$.

Since perturbations are added in the parallel direction of the magnetic field on the top surface of the flux sheet, the Parker mode dominates at long wavelengths ($k_y/k_x = 0$), where the linear analytic growth rate has a relative maximum value iw 0.124 in $kH = 0.275(\lambda = 23H)$.

When $k_y/k_x = 0$, the growth rate is larger in the no shear mode case (a) than that in the shear mode case (b). This is because the interchange mode is coupled in (b), even for $k_y = 0$, since there is a layer where $k_x \perp \mathbf{B}$ in the sheared flux sheet.

On the other hand, the growth rate is generally smaller in (b) than in (a) for short wavelengths. This is because the interchange mode tends to be stabilized by the magnetic tension force in the sheared magnetic field.

Therefore in the case of shear mode (b), the maximum growth rate of $k_y/k_x = 0$ is larger than that of $k_y/k_x = 1, 2$, because the bottom of the sheet is unstable because $k_x \perp \mathbf{B}$.

With $\mathbf{B} = \mathbf{0}$ and $k_y/k_x = 10^{10}$ in the no shear mode case, the growth rate does not have a maximum and increases monotonically with the wavenumber. The growth rate of this case is the same as the pure Rayleigh-Taylor instability which is $a_m\sqrt{kg}$. Here a_m is a parameter of the magnetic interchange instability, and the value of a_m is 0.33.

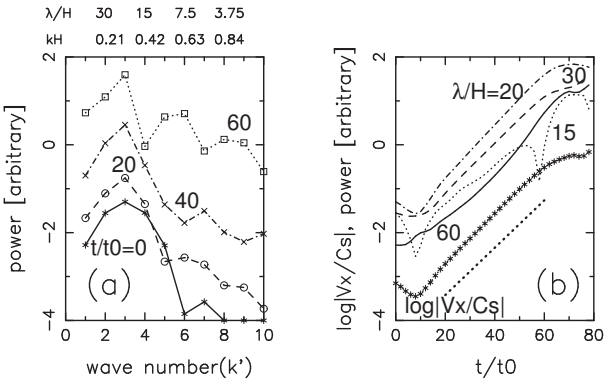

Fig. 20. Time evolution of the x component of the velocity at $z = 0$ for the case shown in model 1. Figure A2a is result of mode analysis. Horizontal axis is wave number ($k(x_{max} - x_{min})/2\pi = k', x_{max} - x_{min} = 60H$) of system and vertical axis is log(power). Full line with $*$ is $t/\tau_0 = 0$, dashed line with $\circ$ is $t/\tau_0 = 20$, dot-dash-dot-dash line with $\times$ is $t/\tau_0 = 40$, dotted line with $\square$ is $t/\tau_0 = 60$. Figure 6b is mode analysis and time evolution of $\log|V_x|$. Full line is $\lambda = 60H(k' = 1, kH = 0.10)$, dashed line is $k' = 2(\lambda = 30H, kH = 0.21)$, dot-dash-dot-dash line is $k' = 3(\lambda = 20H, kH = 0.31)$, dotted line is $k' = 4(\lambda = 15H, kH = 0.42)$, and full line with $*$ is time evolution of $\log|V_x/C_s|$ at the point of $(x, y, z) = (0, 0, 0)$. The dotted line represents the growth rate obtained from linear stability analysis ($i\omega = 0.124$) in $\lambda = 20H(k' = 3, kH = 0.314)$.

A.1.2. 2D Nonlinear Simulations

The horizontal wavelength ($\lambda/H = 20$) of the initial perturbation is close to the wavelength of the maximum growth rate for $= 1$, and the growth rate is 0.12 (see the thick dotted line in figure A2b). Since the perturbation given in the initial condition is not an eigen function, the most unstable wavelength does not grow but other modes are excited by the nonlinear effect.

The above results show that the instability grows on the wavelength given in the initial conditions in the 2D case.

A.1.3. 3D Nonlinear Simulations with Single or Random Perturbations

Figure A3 shows the results in the case of random initial perturbation for both the no shear and shear modes.

It is found that the growth rate in this case is 0.4. Comparing this value with linear theory, we find the corresponding wavenumber is $kH = 1.7(\lambda = 3.7H)$ in $k_y/k_x = \infty$. This $\lambda = 3.7H$ is consistent with $18 \times \Delta x (= \Delta y = 0.2H)$ which agrees with the maximum wavelength resolution of the numerical scheme.

References

Acheson, D. J. 1979, Sol. Phys., 62, 23
Archontis, V., Moreno-Insertis, F., Galsgaard, K., Hood, A., & O'Shea, E. 2004, A&A, 426, 1047
Baierlein, R. 1983, MNRAS, 205, 669
Basu, S., Mouschovias, T. C., & Paleologou, E. V. 1997, ApJL, 480, L55
Born, R. 1974, Sol. Phys., 38, 127

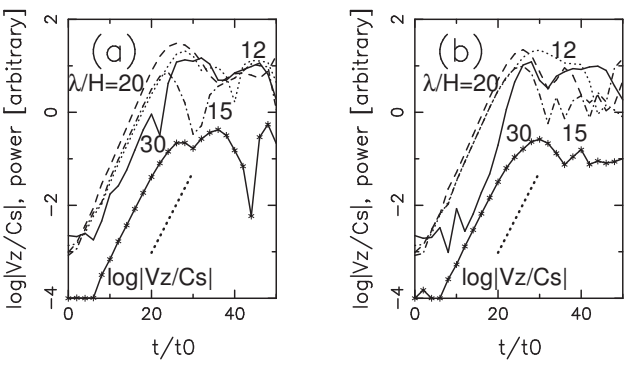

Fig. 21. Time evolution of the z component of the velocity at $(y, z) = (0, 0)$ for the case shown in model 4 and model 5, and other remarks are the same as in figure A2b.

Brandenburg, A., Tuominen, I., Nordlund, A., Pulkkinen, P., & Stein, R. F. 1990, A&A, 232, 277

Brants, J. J. & Steenbeek, J. C. M. 1985, Sol. Phys., 96, 229

Bruzek, A. 1967, Sol. Phys., 2, 451

Bruzek, A. 1969, Sol. Phys., 8, 29

Bumba, V. & Howard, R. 1965, ApJ, 141, 1492

Canfield, R. C. & Fisher, R. R. 1976, ApJL, 210, L149

Cattaneo, F. & Hughes, D. W. 1988, Journal of Fluid Mechanics, 196, 323

Cattaneo, F., Chiueh, T., & Hughes, D. W. 1990, Journal of Fluid Mechanics, 219, 1

Chou, W., Tajima, T., Matsumoto, R., & Shibata, K. 1999, PASJ, 51, 103

Chou, D. & Zirin, H. 1988, ApJ, 333, 420

De Pontieu, B., Erdélyi, R., & James, S. P. 2004, Nature, 430, 536

Defouw, R. J. 1970, ApJ, 160, 659

Fan, Y. 2001, ApJL, 554, L111

Fan, Y., & Gibson, S. E. 2004, ApJ, 609, 1123

Franco, J., Kim, J., Alfaro, E. J., & Hong, S. S. 2002, ApJ, 570, 647

Frazier, E. N. 1972, Sol. Phys., 26, 130

Forbes, T. G. & Priest, E. R. 1984, Sol. Phys., 94, 315

Foglizzo, T. & Tagger, M. 1994, A&A, 287, 297

Galsgaard, K., Moreno-Insertis, F., Archontis, V., & Hood, A. 2005, ApJL, 618, L153

Gilman, P. A. 1970, ApJ, 162,1019

Giz, A. T. & Shu, F. H. 1993, ApJ, 404, 185

Glackin, D. L. 1975, Sol. Phys., 43, 317

Golub, L., Krieger, A. S., & Vaiana, G. S. 1976, Sol. Phys., 49, 79

Golub, L., Krieger, A. S., Harvey, J. W., & Vaiana, G. S. 1977, Sol. Phys., 53, 111

Hachisu, I., Matsuda, T., Nomoto, K., & Shigeyama, T. 1992, ApJ, 390, 230

Hanawa, T., Matsumoto, R., & Shibata, K. 1992, ApJL, 393, L71

Hanami, H. & Tajima, T. 1991, ApJ, 377, 694

Hanasz, M., Otmianowska-Mazur, K., & Lesch, H. 2002, A&A, 386, 347

Harvey, K. L. & Martin, S. F. 1973, Sol. Phys., 32, 389

Harvey, K. L., Harvey, J. W., & Martin, S. F. 1975, Sol. Phys., 40, 87

Heyvaerts, J., Priest, E. R., & Rust, D. M. 1977, ApJ, 216, 123

Horiuchi, T., Matsumoto, R., Hanawa,T., & Shibata, K. 1988, PASJ, 40, 147

Hughes, D. W. & Proctor, M. R. E. 1988, Annual Review of Fluid Mechanics, 20, 187

Hurlburt, N. E., Toomre, J., & Massaguer, J. M. 1986, ApJ, 311, 563

Ishii, T. T., Kurokawa, H., & Takeuchi, T. T. 1998, ApJ, 499, 898

Kaisig, M., Tajima, T., Shibata, K., Nozawa, S., & Matsumoto, R. 1990, ApJ, 358, 698

Kato, S. & Horiuchi, T. 1986, PASJ, 38, 313

Kamaya, H., Mineshige, S., Shibata, K., & Matsumoto, R. 1996, ApJL, 458, L25

Kamaya, H., Horiuchi, T., Matsumoto, R., Hanawa, T., Shibata, K., & Mineshige, S. 1997, ApJ, 486, 307

Kawaguchi, I. & Kitai, R. 1976, Sol. Phys., 46, 125

Kim, J., Hong, S. S., Ryu, D., & Jones, T. W. 1998, ApJL, 506, L139

Kim, J. & Hong, S. S. 1998, ApJ, 507, 254

Kim, J., Franco, J., Hong, S. S., Santillán, A., & Martos, M. A. 2000, ApJ, 531, 873

Kim, J., Ryu, D., & Jones, T. W. 2001, ApJ, 557, 464

Kim, W., Ostriker, E. C., & Stone, J. M. 2002, ApJ, 581, 1080

Kruskal, M. D., & Schwarzchild, M., 1954, Proc. R. Soc. London, Ser. A, 223 ,348

Kundu, M. & Woodgate, B. 1986, Energetic Phenomena on the Sun,

Kurokawa, H. 1987, Sol. Phys., 113, 259

Kurokawa, H. 1988, Vistas in Astronomy, 31, 67

Kurokawa, H. 1989, Space Science Reviews, 51, 49

Kurokawa, H., Wang, T., & Ishii, T. T. 2002, ApJ, 572, 598

Kusano, K., Moriyama, K., & Miyoshi, T. 1998, Physics of Plasmas, 5, 2582

Magara, T., 2004, ApJ, 605, 480

Magara, T. & Longcope, D. W. 2001, ApJL, 559, L55

Magara, T., & Longcope, D. W. 2003, ApJ, 586, 630

Marsh, K. A. 1978, Sol. Phys., 59, 105

Matthews, P. C., Hughes, D. W., & Proctor, M. R. E. 1995, ApJ, 448, 938

Matsumoto, R., Horiuchi, T., Shibata, K., & Hanawa, T. 1988, PASJ, 40, 171

Matsumoto, R., Hanawa, T., Shibata, K., & Horiuchi, T. 1990, ApJ, 356, 259

Matsumoto, R. & Shibata, K. 1992, PASJ, 44, 167

Matsumoto, R., Tajima, T., Shibata,K., & Kaisig, M. 1993, ApJ, 414, 357

Matsumoto, R., Tajima, T., Chou, W., Okubo, A., & Shibata, K. 1998, ApJL, 493, L43

Mouschovias, T. C., Shu, F. H., & Woodward, P. R. 1974, A&A, 33, 73

Newcomb, T. 1961, Phys. Fluids 4, 391

Nozawa, S., Shibata, K., Matsumoto, R., Sterling, A. C., Tajima, T., Uchida, Y., Ferrari, A., & Rosner, R. 1992, ApJS, 78, 267

Nordlund, A. & Dravins, D. 1990, A&A, 228, 155

Parker, E. N. 1955,ApJ, 121,491

Parker, E. N. 1966, ApJ, 145, 811

Parker, E. N. 1974, ApJ, 191, 245

Parker, E. N. 1978, ApJ, 221, 368

Parker, E. N. 1979, Oxford, Clarendon Press; New York, Oxford University Press, 1979

Piddington, J. H. 1975, Ap&SS, 34, 347

Piddington, J. H. 1976a, Ap&SS, 41, 79

Piddington, J. H. 1976b, Ap&SS, 45, 47

Ritchmyer, R. D. & Morton, K. W. 1967, Interscience Tracts in Pure and Applied Mathematics, New York: Interscience, 1967, 2nd ed.,
Rosner, R., Golub, L., & Vaiana, G. S. 1985, ARA&A, 23, 413
Ryu, D., Kim, J., Hong, S. S., & Jones, T. W. 2003, ApJ, 589, 338
Rust, D. M. 1972, Sol. Phys., 25, 141
Rust, D. M. 1994, Geophys. Res. Lett., 21, 241
Schüssler, M. 1990, IAU Symposium, 138, 161
Sheeley, N. R. & Golub, L. 1979, Sol. Phys., 63, 119
Shibata, K. 1980, Sol. Phys., 66, 61
Shibata, K. 1983, PASJ, 35, 263
Shibata, K., Tajima, T., Matsumoto, R., Horiuchi, T., Hanawa, T., Rosner, R., & Uchida, Y. 1989, ApJ, 338, 471
Shibata, K., Tajima, T., Steinolfson, R. S., & Matsumoto, R. 1989, ApJ, 345, 584
Shibata, K., Nozawa, S., Matsumoto, R., Sterling, A. C., & Tajima, T. 1990, ApJL, 351, L25
Shibata, K., Tajima, T., & Matsumoto, R. 1990, ApJ, 350, 295
Shibata, K. & Matsumoto, R. 1991, Nature, 353, 633
Shu, F. H. 1974, A&A, 33, 55
Spruit, H. C. 1974, Sol. Phys., 34, 277
Spruit, H. C. 1979, Sol. Phys., 61, 363
Spruit, H. C. & van Ballegooijen, A. A. 1982, A&A, 106, 58
Spruit, H. C., Nordlund, A., & Title, A. M. 1990, ARA&A, 28, 263
Stein, R. F. & Nordlund, A. 1989, ApJL, 342, L95
Steinolfson, R. S. & Hundhausen, A. J. 1990, J. Geophys. Res., 95, 6389
Tajima, T., Sakai, J., Nakajima, H., Kosugi, T., Brunel, F., & Kundu, M. R. 1987, ApJ, 321, 1031
Tajima, T. & Shibata, K. 1997, Plasma astrophysics / T. Tajima, K. Shibata. Reading, Mass. : Addison- Wesley, 1997.
Tanaka, K. 1987, PASJ, 39, 1
Uchida, Y. & Shibata, K. 1988, Sol. Phys., 116, 291
Wu, C. C. 1987, Geophys. Res. Lett., 14, 668
Weart, S. R. 1970, ApJ, 162, 987
Zirin, H. 1970, Sol. Phys., 14, 328
Zirin, H. 1972, Sol. Phys., 22, 34
Zirin, H. 1974, IAU Symp. 56: Chromospheric Fine Structure, 56, 161
Zirin, H. & Tanaka, K. 1973, Sol. Phys., 32, 173
Zwaan, C. 1985, Sol. Phys., 100, 397
Zwaan, C. 1987, ARA&A, 25, 83